

# Instabilities of buoyancy-driven coastal currents and their nonlinear evolution in the two-layer rotating shallow water model. Part 2. Active lower layer

J. GULA<sup>1†</sup>, V. ZEITLIN<sup>1</sup> AND F. BOUCHUT<sup>2</sup>

<sup>1</sup>Laboratoire de Météorologie Dynamique, ENS and University P. and M. Curie, 24 rue Lhomond, 75231 Paris, France

<sup>2</sup>Laboratoire d'Analyse et de Mathématiques Appliquées, University Paris-Est and CNRS, 5 boulevard Descartes, 77454 Marne-la-Vallée, France

(Received 1 October 2009; revised 13 July 2010; accepted 19 July 2010;  
first published online 22 October 2010)

This paper is the second part of the work on linear and nonlinear stability of buoyancy-driven coastal currents. Part 1, concerning a passive lower layer, was presented in the companion paper Gula & Zeitlin (*J. Fluid Mech.*, vol. 659, 2010, p. 69). In this part, we use a fully baroclinic two-layer model, with active lower layer. We revisit the linear stability problem for coastal currents and study the nonlinear evolution of the instabilities with the help of high-resolution direct numerical simulations. We show how nonlinear saturation of the ageostrophic instabilities leads to reorganization of the mean flow and emergence of coherent vortices. We follow the same lines as in Part 1 and, first, perform a complete linear stability analysis of the baroclinic coastal currents for various depths and density ratios. We then study the nonlinear evolution of the unstable modes with the help of the recent efficient two-layer generalization of the one-layer well-balanced finite-volume scheme for rotating shallow water equations, which allows the treatment of outcropping and loss of hyperbolicity associated with shear, Kelvin–Helmholtz type, instabilities. The previous single-layer results are recovered in the limit of large depth ratios. For depth ratios of order one, new baroclinic long-wave instabilities come into play due to the resonances among Rossby and frontal- or coastal-trapped waves. These instabilities saturate by forming coherent baroclinic vortices, and lead to a complete reorganization of the initial current. As in Part 1, Kelvin fronts play an important role in this process. For even smaller depth ratios, short-wave shear instabilities with large growth rates rapidly develop. We show that at the nonlinear stage they produce short-wave meanders with enhanced dissipation. However, they do not change, globally, the structure of the mean flow which undergoes secondary large-scale instabilities leading to coherent vortex formation and cutoff.

**Key words:** gravity currents, shallow water flows, waves in rotating fluids

---

† Email address for correspondence: gula@lmd.ens.fr

## 1. Introduction

In the companion paper Gula & Zeitlin (2010), which hereafter will be referred to as Part 1, we undertook a detailed analysis of the instabilities of the buoyancy-driven coastal currents (BDCC in what follows) in the framework of the reduced-gravity one-layer rotating shallow water model. We have explained the leading linear instability in terms of resonance between Kelvin waves trapped at the coast, and so-called frontal (Rossby type) waves trapped at the density front, where the current terminates. By initializing the high-resolution direct numerical simulation (DNS) with the most unstable mode, we were able to identify the saturation mechanism of the instability via the Kelvin wave breaking and reorganization of the mean flow which, in turn, leads to secondary instability saturating via frontal wave breaking and formation of coherent vortex structures.

As was already discussed in Part 1, the simple and physically transparent one-layer reduced-gravity model neglects the interactions between the upper layer, where the BDCC evolves, and the lower layer, which is assumed to be completely passive, i.e. infinitely thick. As was also mentioned, the baroclinic effects, arising if the lower layer is active, bring in completely new phenomena related to the interaction of waves propagating in the upper and lower layers. The goal of this paper is, precisely, to study how these new phenomena influence linear and nonlinear stages of instability of the BDCC. We will be globally following the lines of Part 1, by undertaking first an exhaustive linear stability analysis with the help of the collocation method, and then by studying the nonlinear evolution of the developing instability with the help of the high-resolution DNS using a new finite-volume two-layer shallow water scheme (Bouchut & Zeitlin 2010). It should be stressed that while there is no principal difference, in what concerns the collocation approach, between the linear stability analysis in the one-layer and two-layer cases, although calculations become much more cumbersome due to the increased number of dynamical variables for two layers, the difficulty of nonlinear simulations is qualitatively new, as the two-layer system, unlike the one-layer one, is of the mixed type and loses hyperbolicity for strong enough shear between the layers (e.g. LeSommer *et al.* 2003).

In what follows, we will emphasize the new elements brought in by the presence of the active lower layer, without dwelling on phenomena already discussed in Part 1. Although the lower layer is active, we will limit ourselves to configurations where the mean velocity of the lower layer is always zero in linear stability analysis or is initially zero in DNS. Obviously (and this will be a primary consistency check below), the ‘barotropic’ reduced-gravity results of Part 1 should be reproduced in the limit of large thickness of the lower layer. We will be discussing two different configurations: the case of a barotropically stable (in the previous sense) and the case of a barotropically unstable current in the upper layer. In the first case all instabilities are purely baroclinic, while in the second case instabilities of baroclinic origin will be admixed to the leading barotropic instability.

## 2. Buoyancy-driven coastal currents in the two-layer rotating shallow water model and the linear stability problem

In §2, we first recall the two-layer rotating shallow water model and its linearized version, and introduce the key parameters (§2.1). We then display the results of the linear stability analysis by the collocation method: the instabilities, their growth rates and the structure of the unstable modes for a barotropically stable flow (§2.3), and for a barotropically unstable flow (§2.4).

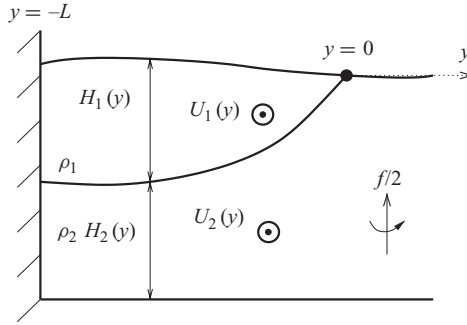


FIGURE 1. Schematic representation of a BDCC in the two-layer model.

### 2.1. An overview of the model

We consider the two-layer BDCC configuration presented in figure 1. It consists of an upper layer of lighter fluid of density,  $\rho_1$ , with a free surface terminating at some point (a density front), a mean steady velocity,  $U_1(y)$ , and a lower layer of density,  $\rho_2 > \rho_1$ , with a mean steady velocity,  $U_2(y)$ . In the examples treated below  $U_2(y)$  will be taken to be zero. The equations of two-layer rotating shallow water are

$$\left. \begin{aligned} D_j u_j - f v_j &= -\frac{1}{\rho_j} \partial_x \pi_j, \\ D_j v_j + f u_j &= -\frac{1}{\rho_j} \partial_y \pi_j, \\ \partial_t h_j + \nabla \cdot (h_j \mathbf{v}_j) &= 0, \end{aligned} \right\} \quad (2.1)$$

where the index  $j = 1, 2$  denotes the upper and the lower layers, respectively,  $(x, y)$  and  $\mathbf{v}_j = (u_j, v_j)$  are the zonal and meridional coordinates and velocity components, respectively,  $h_j(x, y, t)$  are the depths of the layers,  $\pi_j, \rho_j$  are the pressures and the densities of the layers, respectively,  $D_j = \partial_t + u_j \partial_x + v_j \partial_y$  is the Lagrangian derivative and  $f$  is the constant Coriolis parameter. The pressures in the upper and lower layers are related to the depths of the layers via the hydrostatic balance relations

$$\nabla \pi_j = \rho_j g \nabla (s^{j-1} h_1 + h_2), \quad (2.2)$$

where  $s = \rho_1/\rho_2$  is the stratification parameter and  $g$  is the gravity. We linearize these equations about the steady geostrophically balanced state with the depth profiles  $H_j(y)$  and corresponding velocities  $U_j(y)$

$$\partial_y H_j = (-1)^{j-1} \frac{f}{g'} (U_2 - s^{j-1} U_1), \quad (2.3)$$

where  $g' = (1 - s)g$  is the reduced gravity. The linearized equations, where  $u_j, v_j$  and  $h_j$  are the perturbations to the basic state fields, are as follows:

$$\left. \begin{aligned} \partial_t u_j + U_j \partial_x u_j + v_j \partial_y U_j - f v_j &= -g \partial_x (s^{j-1} h_1 + h_2), \\ \partial_t v_j + U_j \partial_x v_j + f u_j &= -g \partial_y (s^{j-1} h_1 + h_2), \\ \partial_t h_j + U_j \partial_x h_j + H_j \partial_x u_j &= -\partial_y (H_j v_j). \end{aligned} \right\} \quad (2.4)$$

In order to compare our results with those of the reduced-gravity configuration of Part 1, the setting and the non-dimensionalization are chosen in the same way. We introduce the time scale  $f^{-1}$ , the horizontal scale  $L$ , which is the unperturbed width

of the current, the velocity scale  $fL$  and the vertical scale  $(fL)^2/g'$ . We will use only non-dimensional variables from now on without changing notation. The linearized equations thus are as follows:

$$\left. \begin{aligned} \partial_t u_j + U_j \partial_x u_j + v_j \partial_y U_j - v_j &= -\partial_x \left( \frac{s^{j-1} h_1 + h_2}{1-s} \right), \\ \partial_t v_j + U_j \partial_x v_j + u_j &= -\partial_y \left( \frac{s^{j-1} h_1 + h_2}{1-s} \right), \\ \partial_t h_j + U_j \partial_x h_j + H_j \partial_x u_j &= -\partial_y (H_j v_j). \end{aligned} \right\} \quad (2.5)$$

The important parameters in what follows are  $U_0$ , the non-dimensional velocity of the upper layer at the front location ( $y=0$ ), which is in fact equivalent to a Rossby number, the density ratio  $s = \rho_1/\rho_2$  and the depth ratio  $r = H_2(y_0)/H_1(y_0)$ , where  $y_0$  is defined by  $H_1(y_0) = \max(H_1)$ .

The boundary condition of no normal flow at the wall is the same as in the one-layer case for both layers:  $v_j(-1) = 0$ .

The boundary condition at the front for the upper layer is also the same as in the one-layer case, because the only constraint to be imposed is the regularity of  $(u_1, v_1, h_1 + h_2)$  at  $y=0$ .

For solutions harmonic in the  $x$ -direction

$$(u_j(x, y), v_j(x, y), h_j(x, y)) = (\tilde{u}_j(y), \tilde{v}_j(y), \tilde{h}_j(y)) \exp[i(kx - \omega t)], \quad (2.6)$$

$\pi_2$  satisfies the equation  $\partial_{yy} \pi_2 = k^2 \pi_2$  in the half-plane  $y > 0$  with no upper layer. Hence, the solution which decays away from the free streamline at  $y \rightarrow \infty$  has to satisfy the equation  $\partial_y \pi_2 = -k \pi_2$  (we thus exclude from our analysis the modes coupled to free gravity waves far from the front). In order for the solution of  $\pi_2$  in the region  $y < 0$  to match continuously the decaying solution for  $y > 0$ , we require that the two are identical at  $y=0$ . Thus the boundary conditions at the front for the lower layer give (see Paldor & Killworth 1987 for details):

$$\partial_y (s h_1 + h_2) = -k (s h_1 + h_2) \quad \text{at } y = 0. \quad (2.7)$$

Assuming (2.6), we obtain an eigenvalue problem of order 6 which can be solved by applying the spectral collocation method as described in Trefethen (2000) and Poulin & Flierl (2003), along the same lines as in Part 1.

In the following, we will consider a bottom layer initially at rest ( $U_2 = 0$ ) and an upper flow with constant potential vorticity (PV). The constant PV in the upper flow corresponds to the solution of the equation  $1 + H_{1yy} - Q_1 H_1 = 0$ , which gives

$$U_1(y) = U_0 \cosh(\sqrt{Q_1} y) + \frac{1}{\sqrt{Q_1}} \sinh(\sqrt{Q_1} y), \quad (2.8)$$

$$H_1(y) = -\frac{1}{Q_1} [1 - \sqrt{Q_1} U_0 \sinh(\sqrt{Q_1} y) - \cosh(\sqrt{Q_1} y)], \quad (2.9)$$

$$H_2(y) = (r + s) \max(H_1) - s H_1(y), \quad (2.10)$$

where  $Q_1$  is the constant PV of the mean flow in the upper layer and  $U_0 = U_1(0)$  is the current velocity of the upper layer at the front. Note that the bottom layer initially at rest ( $U_2 = 0$ ) implies a variable PV in this layer of the form

$$Q_2(y) = \left[ (r + s) \max(H_1) + \frac{s}{Q_1} [1 - \sqrt{Q_1} U_0 \sinh(\sqrt{Q_1} y) - \cosh(\sqrt{Q_1} y)] \right]^{-1}. \quad (2.11)$$

It should be emphasized that this basic state never satisfies Ripa's criterion (Ripa 1991), which states that sufficient conditions for stability are

$$\exists \alpha / \forall y \left\{ \begin{array}{l} (U_j - \alpha) \frac{dQ_j}{dy} \leq 0 \quad (j = 1, 2), \\ \frac{(U_1 - \alpha)^2}{H_1} + \frac{(U_2 - \alpha)^2}{H_2} \leq g'. \end{array} \right. \quad (2.12)$$

Indeed, an inspection of (2.12) shows that:

- (i) The first condition is always satisfied for the upper layer as  $Q_1 = \text{constant}$ .
- (ii) The first condition for the lower layer gives  $\alpha U_1 / H_2^2 \leq 0$ , which could be satisfied only for  $[\alpha = 0]$  or  $[\alpha \leq 0 \text{ and } U_1(y) \geq 0]$  or  $[\alpha \geq 0 \text{ and } U_1(y) \leq 0]$ , considering that  $H_2$  stays finite.
- (iii) Due to the presence of the front at  $y=0$  ( $H_1(0)=0$ ), the second condition can be satisfied only for  $\alpha = U_1(0)$ , which is not compatible with previous conditions. Hence, it is impossible to satisfy both criteria for this basic state, except in the limit  $H_2 \rightarrow +\infty$  where we recover the one-layer condition for stability (cf. Part 1).

## 2.2. Instabilities and resonances between the eigenmodes

As in the one-layer configuration of Part 1, the instabilities of the BDCC in the two-layer case originate from resonances between the eigenmodes of the linearized problem (crossing of dispersion curves for different types of waves, cf. Cairns 1979). The wave species of the rotating shallow water models are Poincaré (inertia gravity) modes, Rossby modes (if PV gradients are present), unidirectional Kelvin modes trapped at the boundary, in the bounded domains, and frontal modes trapped in the vicinity of the free streamlines (outcropping/incropping lines). We do not discuss topographic effects here, which would significantly increase the variety of wave species (cf. Leblond & Mysak 1978).

For the two-layer BDCC configuration with constant PV in the upper layer, which is the subject of the present work, we thus have Poincaré and Kelvin waves in both layers, Rossby waves in the lower layer, as the PV is not held constant there, and a frontal wave in the upper layer. The instabilities which have been discussed previously in the literature for this configuration are related to the following resonances: (a) the resonance of a Kelvin or a Poincaré mode with a frontal mode in the upper layer, which has already been discussed in the reduced-gravity model in Part 1; (b) the baroclinic resonance between a frontal mode in the upper layer and a Rossby mode in the lower layer (Killworth, Paldor & Stern 1984; Kubokawa 1988; Barth 1989), which is sometimes confused with the classical baroclinic instability, or is called mixed barotropic/baroclinic instability due to its energetics; (c) high wavenumber resonances between a Poincaré wave in the lower layer and a frontal or Poincaré wave in the upper layer, all of them giving shear instabilities with features similar to the classical Kelvin–Helmholtz (KH) instability (Paldor & Ghil 1991).

Other resonances are *a priori* also possible, but were not discussed in the literature in this context, to our knowledge: (a) the resonance between a Kelvin or Poincaré wave in the upper layer and a Rossby wave in the lower layer, which is usually called Rossby–Kelvin instability (RK) as discussed in Sakai (1989) and Gula, Plougonven & Zeitlin (2009a); (b) the resonance between a Kelvin wave in the lower layer and the frontal wave in the upper layer, which would be similar to the RK instability at low wavenumbers and to the vertical shear instability at high wavenumbers. We will demonstrate below that these resonances are indeed relevant.

Two main configurations will be discussed in the following sections. We will first study a barotropically stable basic state (stable in the reduced-gravity model) and

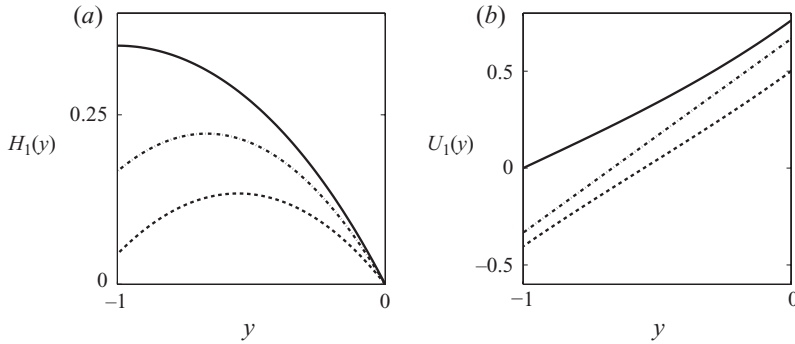


FIGURE 2. Examples of basic state depths (a) and velocities (b) for a constant PV flow in the upper layer with  $Q_1 = 1$  and  $U_0 = -\tanh(-1)$  (thick line),  $Q_1 = 1$  and  $U_0 = 1/2$  (dotted line) and a zero-PV flow (dash-dotted line).

then a barotropically unstable basic state (unstable with respect to the frontal-Kelvin instability in the upper layer discussed in Part 1). We will present an exhaustive linear stability analysis and identify the resonances leading to instabilities in both cases.

### 2.3. Unstable modes of a barotropically stable flow

We first consider a basic flow with zero velocity at the wall (cf. figure 2). This configuration corresponds to a flow with constant PV ( $Q_1 = 1$ ) without reversal of velocity in the upper layer, and hence barotropically stable, as was shown in Part 1. Figure 3 displays dispersion diagrams for the phase speeds and growth rates of the eigenmodes as functions of the wavenumber  $k$  for the decreasing values of the depth ratio  $r = 100, 10, 2, 0.5, 0.1$  at stratification parameter  $s = 0.5$ . Compared to the one-layer case, several new features are manifest.

First, a new dispersion curve  $kc = 1$  denoted by  $I$  in the figure appears. It corresponds to inertial motion in the lower layer, with the quiescent upper layer, as follows from figure 4 where the velocity and pressure fields in both layers are presented. The clearly visible absence of pressure variations is typical for inertial oscillations. This mode was already discussed in Paldor & Ghil (1991). Again, as seen from figure 4, it is a lower-layer motion, which explains the absence of the corresponding curve in the one-layer dispersion diagram of Part 1. In spite of intersections of this curve with other branches of the dispersion diagram, no resonances, and hence no instabilities between the inertial motion and other modes arise due to its pressureless character. Indeed, pressure fluctuations are required for the instability to arise (Cairns 1979), as the coupling between the layers, necessary for the resonance between upper- and lower-layer waves, is achieved through pressure (cf. the instability criterion in Sakai 1989).

Second, a bunch of dispersion curves with  $c \approx 0$ , which are all collapsed into a single line denoted by  $R$  in figure 3, arises. A sequence of close dispersion curves is seen if zoomed in, cf. figure 5. It corresponds to a set of Rossby modes in the lower layer, of different structure in the direction perpendicular to the coast, arising due to the variations of PV imposed by the inclined interface. These Rossby modes can resonate with the frontal mode and the Poincaré modes and produce instabilities even for large  $r$ , as seen from figure 5. Yet, growth rates of these instabilities are indeed very small and the intervals of unstable wavenumbers are very narrow for large  $r$ .

Figure 3(b,c), corresponding to  $r = 10$  and  $r = 2$ , respectively, shows two well-formed zones of instability that can be easily interpreted by looking at the dispersion curves for the corresponding modes. The first instability ( $k < 1$ ) results from the

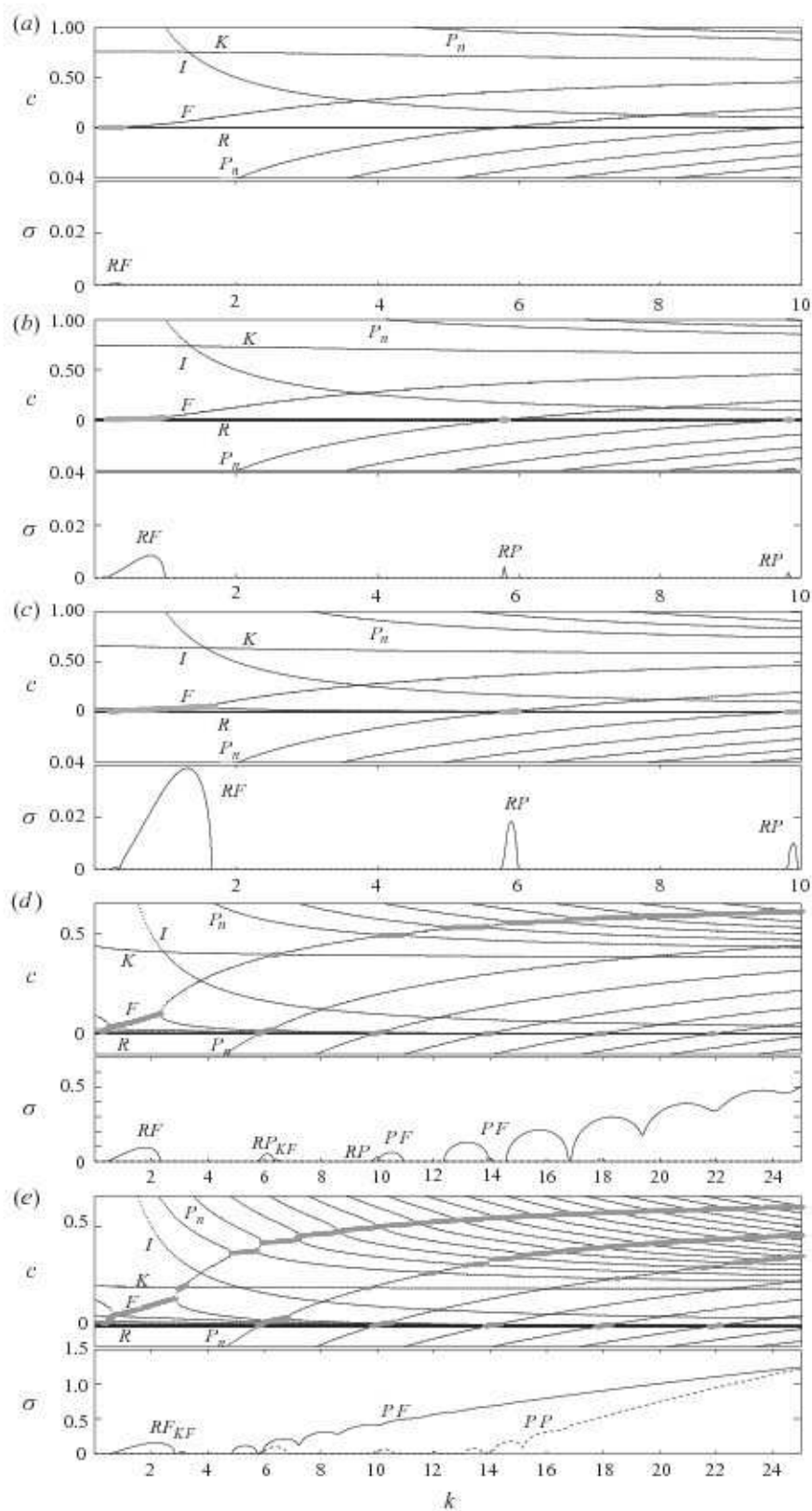


FIGURE 3. For caption see next page.

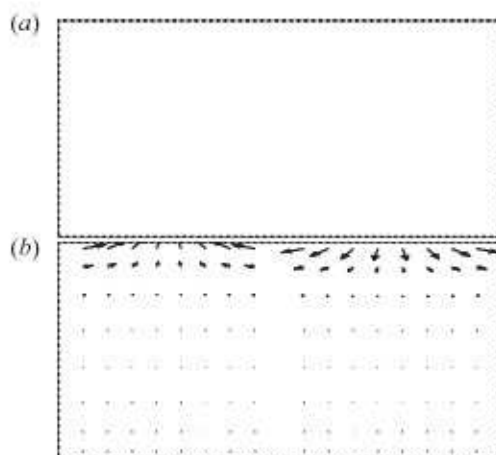


FIGURE 4. Pressure and velocity fields of the inertial mode in the upper layer (a) and in the lower layer (b) corresponding to the dispersion curve  $kc = 1$  for  $k = 10$  and  $r = 100$ . Maximum value for  $u_2$  and  $v_2$  is 0.8, while  $u_1$ ,  $v_1$ ,  $\pi_1$  and  $\pi_2$  are of order  $10^{-6}$  or less and hence are not visible in the figure.

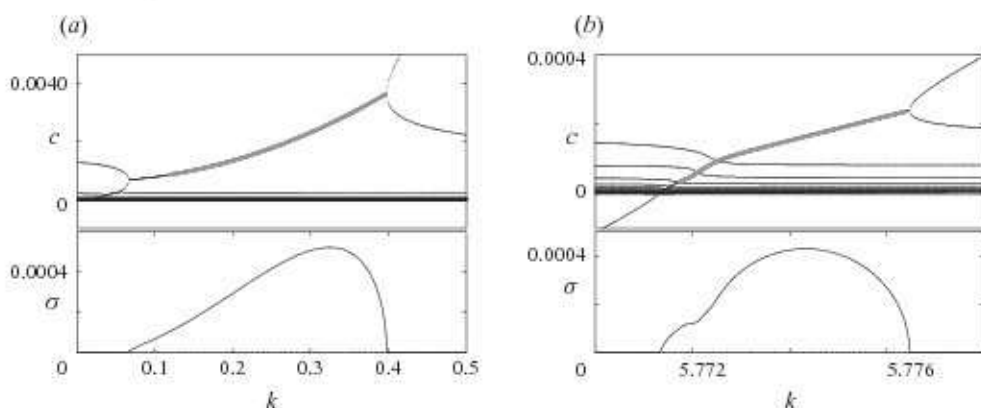


FIGURE 5. Zoom of the RF instability part (a) and RP instability part (b) of figure 3(a).

already mentioned resonance between a Rossby wave in the lower layer and the frontal mode in the upper layer. The corresponding pressure and velocity fields in both layers are plotted in figure 6(a) and confirm this interpretation.

The Rossby eigenmodes are absent in the upper layer owing to the uniformity of PV. They are replaced by a continuous spectrum of singular modes, which do not interact with the modes in the lower layer as explained, e.g. in Iga (1997). However, as was already discussed in Part 1, the frontal mode has the characteristics of a Rossby wave for low wavenumbers, and the unstable mode under consideration is therefore very similar to the classical baroclinic instability which can be described as the interaction between two Rossby waves propagating in each layer (see Hoskins, McIntyre & Robertson 1985). It is interesting to note that the uniform PV in the

FIGURE 3. Dispersion diagrams of the barotropically stable current with  $Q_1 = 1$  corresponding to the basic state profile with constant PV in the upper layer and  $s = 0.5$ . The depth ratios between the lower and the upper layer are as follows: (a)  $r = 100$ , (b)  $r = 10$ , (c)  $r = 2$ , (d)  $r = 0.5$  and (e)  $r = 0.1$ . The horizontal scale of (d, e) was shrunk to show the appearance of short-wave vertical shear instabilities.



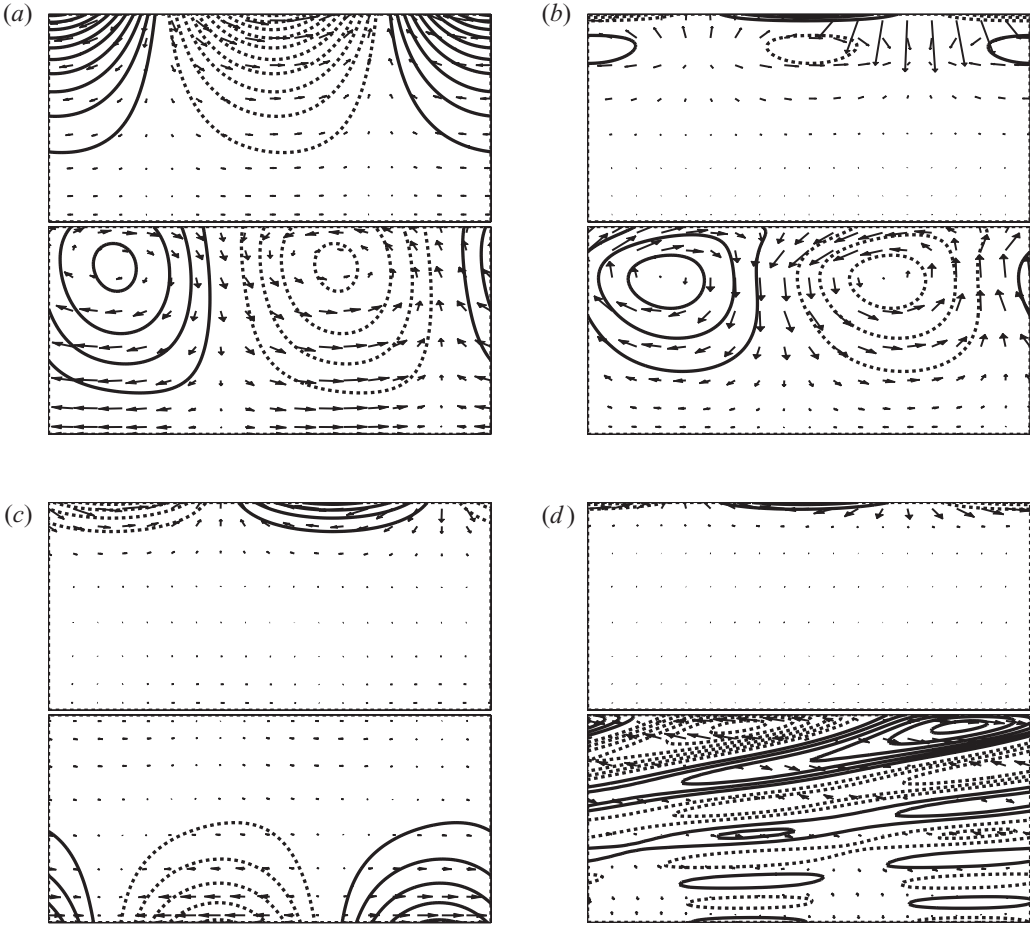


FIGURE 6. Pressure and velocity fields of the typical unstable modes of the barotropically stable current: (a) Rossby mode in the lower layer and the frontal mode in the upper layer (RF instability), (b) Rossby mode in the lower layer and the first Poincaré mode in the upper layer (RP instability), (c) Kelvin mode in the lower layer and frontal mode in the upper layer (KF instability) and (d) Poincaré mode in the lower layer and the frontal mode in the upper layer (PF instability). Pressure contours at the interval 0.015 in the lower layer and at the interval 0.05 in the upper layer. Here and below the full lines correspond to positive and the dotted lines to negative values. Upper (lower) graph in (a–d): upper (lower) layer.

upper layer does not satisfy the Charney–Stern theorem of the PV gradient inversion between the two layers. Hence, this instability has been interpreted as ageostrophic by numerous previous authors, but it is also possible to interpret it as an extension of a QG instability (see a discussion of this point in Boss, Paldor & Thompson 1996). We will call it RF in what follows.

The second instability corresponds to Poincaré modes in the upper layer resonating with a Rossby wave in the lower layer. The pressure and velocity fields for the second unstable mode are plotted in figure 6(b), and confirm this interpretation. Note that the same instability appears at higher  $k$  for Poincaré modes of higher order with decreasing growth rates. We will call this instability RP. Note that this instability is often confused with RK instability, as in Sakai (1989).

Figure 3(d), corresponding to  $r = 0.5$ , displays a new zone of instability at  $k = 6.25$  with low growth rates corresponding to the interaction between the Kelvin mode in

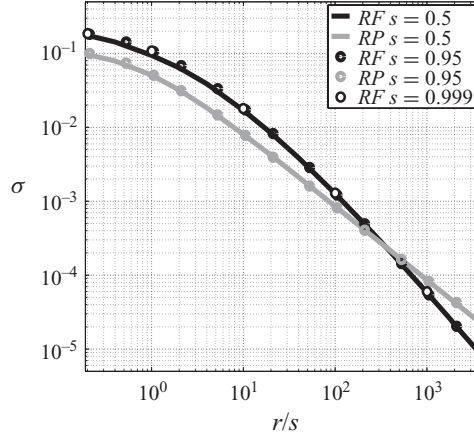


FIGURE 7. Maximum growth rates for the RF instability (black) and RP instability (grey) as a function of the ratio between the depth and density ratios  $r/s$  for  $s=0.5$  (thick line),  $s=0.95$  (full circles) and  $s=0.999$  (empty circles).

the lower layer and the frontal mode in the upper layer, which is plotted in figure 6(c), but above all it displays several new zones of instability at higher wavenumbers with very high growth rates. These are due to the interaction of the frontal mode in the upper layer with various Poincaré modes in the lower layer. This short-wave instability is analogous to the one described by Paldor & Ghil (1991) for the zero-PV case. The frontal mode has the characteristics of a gravity wave for high wavenumbers, this instability is therefore very similar to the vertical shear instability. The pressure and velocity fields for the first Poincaré mode in the lower layer are plotted in figure 6(d). Such instabilities will be called PF.

Figure 3(e), corresponding to  $r=0.1$ , is similar, with the addition of resonances between Poincaré modes in the lower and the upper layers corresponding to vertical shear instability, which may be also called PP to stress its origin (cf. Sakai 1989).

Here we have presented the results of the stability analysis at varying  $r$  and fixed  $s$ . It is easy to repeat it for fixed  $r$  and varying  $s$  (not shown). Not surprisingly, increasing (decreasing)  $s$  has destabilizing (stabilizing) influence. To give an idea of the  $s$  dependence of the growth rates, we plotted the dependence of the growth rates of RF and RP instabilities on the ratio  $r/s$  for different values of  $s$  in figure 7. Not only the growth rates, but also the structure of the eigenmodes and the dispersion diagram as a whole do not vary as long as the ratio  $r/s$  stays the same. Discrepancies appear only for very low depth ratios,  $r \rightarrow 0$ , or very low stratification ratios  $s \rightarrow 0$ .

Let us summarize the linear stability analysis of the barotropically-stable two-layer BDCC. For lower layers deeper than the upper layer, the flow displays two types of baroclinic instabilities: a long-wave RF one and a shorter-wave RP one. Both are extremely weak and of negligible measure in  $k$ -space for large depth ratios, but become more and more vigorous when the depth ratio is decreasing, having comparable growth rates. When the lower layer becomes of the order of, or shallower than the upper one, a series of intense short-wave vertical shear instabilities appear.

#### 2.4. Unstable modes of the barotropically unstable flow

We now consider a barotropically unstable basic flow. The basic state in the upper layer is now unstable, as given in Part 1. Figure 8 shows phase speeds and

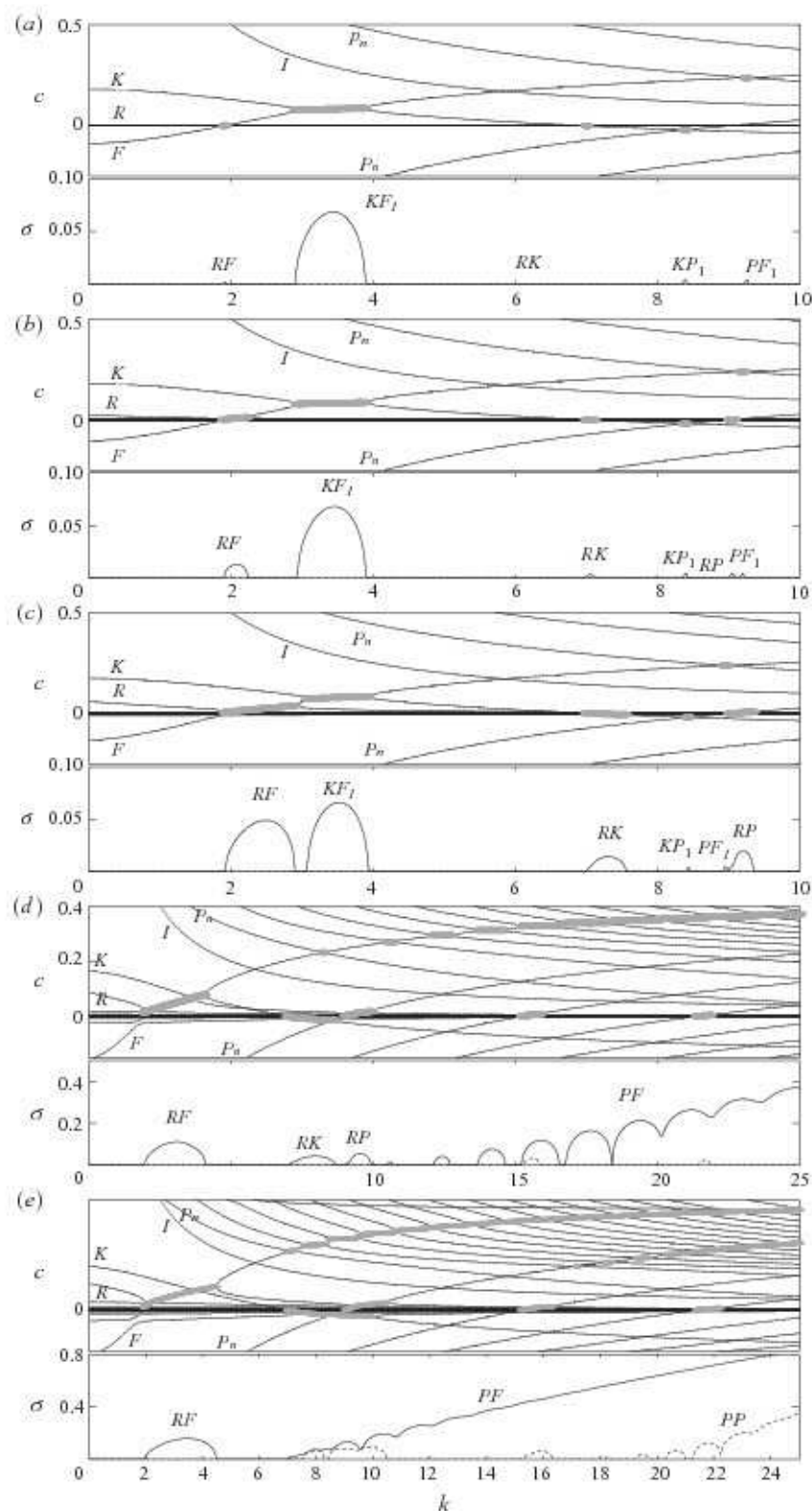


FIGURE 8. For caption see next page.

corresponding growth rates of the eigenmodes as functions of the wavenumber  $k$  for decreasing values of the depth ratio  $r = 100, 10, 2, 0.5, 0.1$ .

We recover the one-layer results when  $r \rightarrow \infty$  (cf. figure 4 in Part 1 and figure 8a), with the main resonance between the Kelvin mode and the frontal mode in the upper layer (KF1) and other instability zones at wavenumbers higher than 8, with much lower growth rates, corresponding to the resonance of the Kelvin mode and the first frontally trapped unbalanced Poincaré mode (KP1), and the interaction of the first coastally trapped Poincaré mode with the balanced frontal mode (PF1), respectively, as already mentioned in Part 1.

The pressure and velocity fields of the related unstable KF1 mode in the upper layer are plotted in the upper graph of figure 9(a), and show absolute coincidence with the corresponding mode of Part 1. Note that related pressure perturbations in the lower layer (see lower graphs in figure 9) are at least one order of magnitude smaller than in the upper one for all instabilities, except for PP and PF ones (see figure 9e,f).

As the depth ratio decreases, the wavenumbers and growth rates for these unstable modes stay quasi-identical, but in parallel, as in the previous case, new instabilities appear due to the baroclinic resonances between a wave in the lower layer and a wave in the upper layer.

Figure 8(a–c), corresponding to  $r = 100, 10, 2$ , respectively, shows three new zones of instability as compared to the one-layer case. They can be easily interpreted by looking at the dispersion curves of the corresponding eigenmodes. The first instability zone (from left to right on the wavenumber axis) is due to the resonance between a Rossby wave in the lower layer and the frontal mode in the upper layer, as in the previous barotropically stable case (RF instability). The corresponding pressure and velocity fields are plotted in figure 9(b). (Slight differences with respect to the similar mode presented in figure 6(a) are due to the difference in the mean flow profile.) The second instability zone corresponds to the upper layer KF instability mode which was already discussed above. The third instability zone corresponds to the resonance between a Rossby mode in the lower layer and a Kelvin mode in the upper layer, which is usually called RK instability (see Sakai 1989; Gula *et al.* 2009a). Note that this unstable mode was not present in the previous case of zero zonal velocity at the wall. The corresponding pressure and velocity fields are plotted in figure 9(c). The fourth instability zone, as in the barotropically stable case, corresponds to the resonance between a Rossby wave in the lower layer and a Poincaré mode in the upper layer (RP instability which is often confused with RK instability). The pressure and velocity fields for this mode are plotted in figure 9(d).

Figure 8(d,e), corresponding to  $r = 0.5$  and  $r = 0.1$ , displays new zones of instability at higher wavenumbers, as in the barotropically stable case. These are due to the interaction of the frontal mode in the upper layer with various Poincaré modes in the lower layer (PF) and to the interaction between Poincaré modes in the lower layer and the upper layer (PP). Examples of such unstable PF and PP modes can be found in figure 6(e,f), respectively. For high wavenumbers, the frontal mode behaves like a Poincaré (gravity) mode and the PF mode has then the properties of the vertical shear instability.

---

FIGURE 8. Dispersion diagrams of the barotropically unstable flow with constant PV in the upper layer  $Q_1 = 1$  and  $s = 0.5$ . The depth ratios between the lower and the upper layer are as follows: (a)  $r = 100$ , (b)  $r = 10$ , (c)  $r = 2$ , (d)  $r = 0.5$  and (e)  $r = 0.1$  corresponding to black squares in figure 10. The horizontal scale of (d,e) was shrunk to show the appearance of vertical shear instabilities.

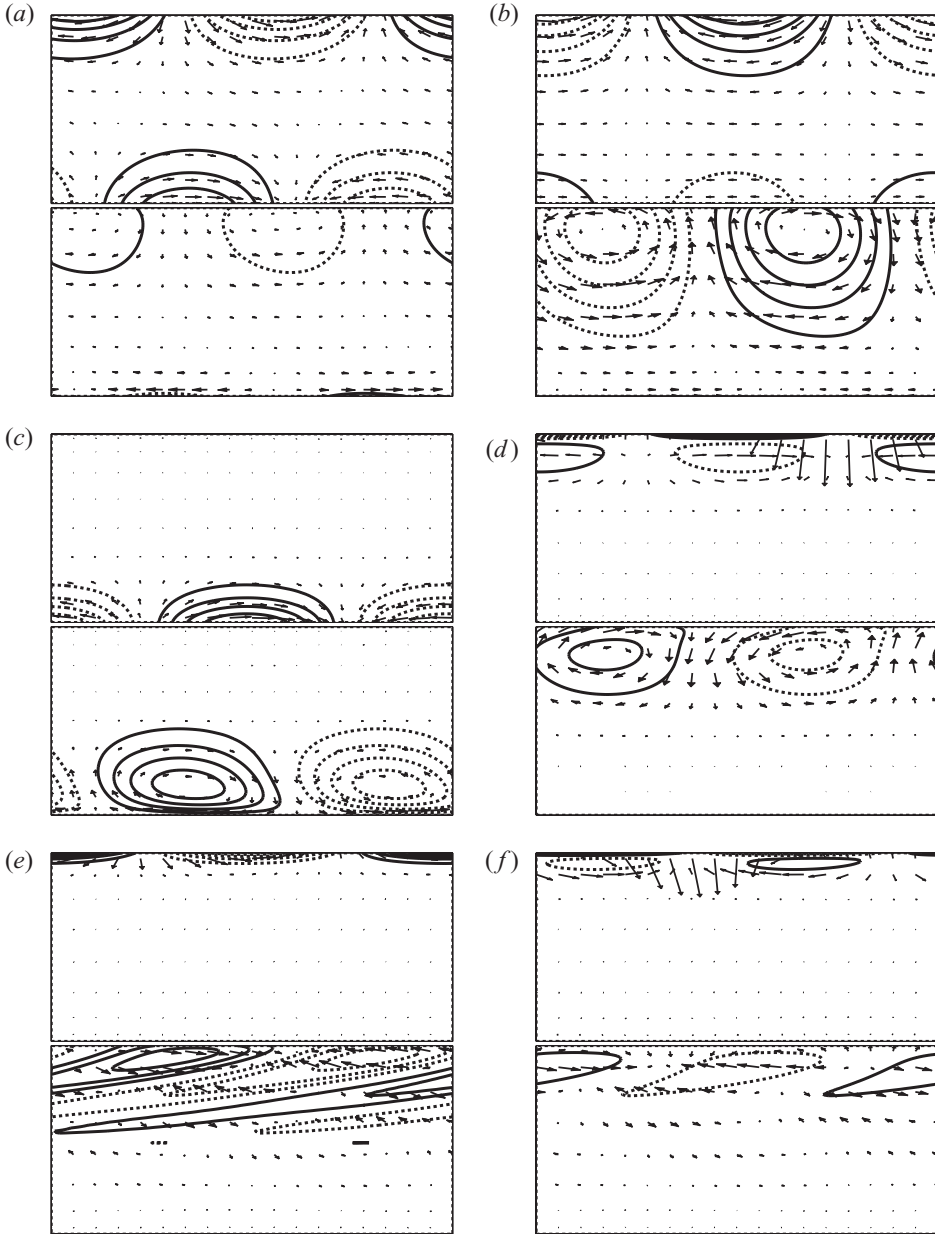


FIGURE 9. Pressure and velocity fields of the typical unstable modes for the barotropically unstable coastal current. (a) Resonance between a Kelvin mode and the frontal mode in the upper layer (corresponding to the frontal KF instability in the reduced-gravity model), (b) resonance between a Rossby mode in the lower layer and the frontal mode (RF instability), (c) resonance between a Rossby mode in the lower layer and a Kelvin wave in the upper layer (RK instability), (d) resonance between a Rossby mode in the lower layer and the first Poincaré mode in the upper layer (RP instability), (e) resonance between a Poincaré mode in the lower layer and the frontal mode in the upper layer (PF instability) and (f) resonance between a Poincaré mode in the lower layer and a Poincaré mode in the upper layer (PP instability). Pressure contours interval is 0.1 in the upper layer for all panels, and pressure contours interval in the lower layer is 0.001 for (a) and (b), 0.0005 for (c) and (d) and 0.05 for (e) and (f). Upper (lower) graph in (a–f): upper (lower) layer.

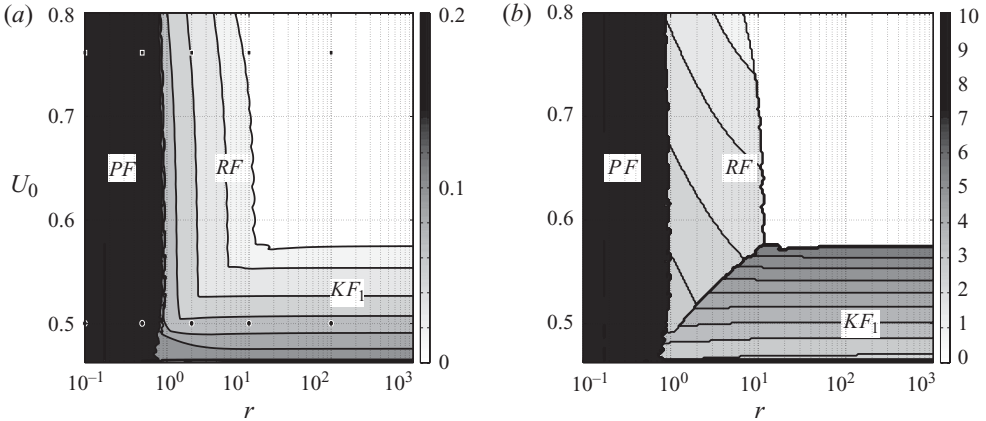


FIGURE 10. Stability diagram in  $U_0$ - $r$  space for growth rates (a) and wavenumbers (b) of the unstable modes for  $Q_1 = 1$  and  $s = 0.5$ . Black dots correspond to the values of the aspect ratio used in the dispersion diagrams above. Location of typical instabilities: PF, RF and  $KF_1$  in the parameter space is indicated by inserts.

Let us summarize the results of the linear stability analysis for the barotropically-unstable two-layer BDCC. For very deep lower layers the only instability is the upper-layer KF instability of the one-layer reduced-gravity approximation. When the depth of the lower layer diminishes, the upper-layer KF instability remains dominant, but RF and RK/RP instabilities appear with, respectively, lower and higher characteristic wavenumbers. For lower layers of depth comparable to or smaller than the upper one vigorous short-wave vertical shear (i.e. PF and PP) instabilities appear.

### 2.5. Synthetic stability diagrams

We finally give full stability diagrams for the BDCC at fixed  $s = 0.5$  in the Rossby number – depth ratio space for growth rates and corresponding wavenumbers of the unstable modes in figure 10. Note that the diagram does not substantially vary for larger values of  $s$  (not shown). Shear instabilities with high growth rates dominate at all scales at small  $r$  and the barotropic  $KF_1$  instability, if any, dominates at large  $r$ .

## 3. Nonlinear evolution of unstable modes

Following the same philosophy as in Part 1, we will investigate in §3 the nonlinear evolution of the instabilities identified from the linear stability analysis. For this, we need adequate numerical tools. As was already mentioned in §1, the two-layer shallow water equations represent a system of mixed type, with transitions from hyperbolicity to ellipticity which are, generally, very difficult to treat numerically. Physically, the loss of hyperbolicity in the two-layer shallow water system corresponds to the onset of vertical shear instability, which has common features with the KH instability and is widely described as such in the literature (see e.g. LeSommer *et al.* 2003). Although of a similar physical nature, it is not equivalent to the classical KH instability in the two-layer Euler equations, by construction of the two-layer shallow water model. We use therefore a denomination ‘vertical shear instability’ for such instability related to the loss of hyperbolicity of the equations in what follows. Another difficulty is the lack of a conservation law, since only the total momentum is conserved in the system, but not the momentum of each layer separately. This implies the lack of a unique

set of Rankine–Hugoniot conditions for the weak solutions of the system, see the discussion below.

A recently proposed new well-balanced scheme for multi-layer shallow water equations (Bouchut & Zeitlin 2010), is the first which treats the loss of hyperbolicity in a satisfactory manner. In what follows, we will implement this scheme, with inclusion of rotation along the lines of Bouchut, Le Sommer & Zeitlin (2004), in order to analyse nonlinear evolution of the unstable BDCC.

We first sketch the properties of the multi-layer version of the high-resolution well-balanced finite-volume numerical scheme in §3.1. We then study the nonlinear development of a perturbation for a barotropically stable flow in §3.2 and the non-linear evolution of the most unstable mode for a barotropically unstable flow in §3.3.

### 3.1. *A well-balanced entropy satisfying finite-volume scheme for the multi-layer rotating shallow-water model*

The method of Bouchut & Zeitlin (2010) is based on the idea of operator splitting for the multi-layer shallow water equations, already implemented in Bouchut & Morales (2008). It consists in solving the equations successively layer by layer and treating the interfaces between the layers as effective topography for the layer under resolution. The method has the following advantages: (a) if the resolution for each layer is performed with a well-balanced sub-scheme, the whole scheme is well balanced; (b) if the resolution for each layer is performed with an entropy-satisfying sub-scheme, the whole scheme is entropy-satisfying, i.e. the total energy is decreasing through shocks; (c) the scheme is non-negative in level thicknesses, and allows for ‘drying’ of layers; (d) no estimate of the eigenvalues of the whole system (which become complex when the hyperbolicity is lost) is needed, the scheme is always consistent and one can use the Courant–Friedrichs–Lewy (CFL) conditions associated with each subsystem. A variant of the splitting scheme allowing the solution simultaneously, and not successively, for all layers, a ‘sum scheme’ (cf. Bouchut & Zeitlin 2010), is applied, with an upwind corrected hydrostatic reconstruction scheme and relaxation solver. A second-order reconstruction scheme in space is used, together with a two-step Heun scheme in time. The two-dimensional aspects are treated direction by direction.

A natural question arises in the context of any shock-capturing numerical scheme, including the present one: what are the Rankine–Hugoniot (RH) conditions it corresponds to? This question is automatically answered in the one-layer version of our code, used in Part 1. Indeed, as is well known (cf. e.g. Whitham 1974), the standard RH conditions for the one-layer rotating shallow-water model follow from the momentum and mass conservation and satisfy the energy decrease constraint, which replaces the entropy increase constraint across the shocks in gas dynamics. The entropy inequalities are built into our numerical scheme, which is one of its major advantages, so the standard RH conditions are ensured.

The situation is more complicated in the two-layer rotating shallow-water model. The system of conservation laws in this case is not sufficient to uniquely determine RH conditions at the shocks at the interface between the layers since the system is non-conservative, see Klemp, Rotunno & Skamarock (1997) and references therein for a discussion in the physical and, e.g. Castro *et al.* (2008), in the mathematical context. Different choices of RH conditions correspond to different dominant physical processes at the interface, which may be rather complex (cf. Klemp *et al.* 1997). The above-mentioned possible loss of hyperbolicity related to the onset of the shear instability also reflects the complexity of the interfacial processes. Obviously, models more complicated than the two-layer models are needed to resolve these processes,

the first step may be e.g. the three-layer ones with an intermediate buffer layer (e.g. Lyapidevsky & Teshukov 2000).

Our intention is not to dwell on the details of parametrizations of the physical processes at the interface, but to fully exploit the efficient high-resolution scheme of Bouchut & Zeitlin (2010), and its ability to ‘go through’ the ellipticity zones which manifest themselves just as enhanced dissipation zones, as will be shown below. As to the RH conditions our scheme with the centred discretization is consistent with the standard RH conditions for shallow-water (cf. Whitham 1974) layerwise, as follows from Bouchut & Zeitlin (2010, equation (25)). In our two-dimensional context, these RH conditions can be written as follows.

Let  $(n_t, \mathbf{n})$  be a normal to an hyper-surface of discontinuity in time space, and denote by  $[\dots]$  the jump of a quantity through this hyper-surface. Then the RH condition associated to the continuity equation is

$$[h_j]n_t + [h_j \mathbf{v}_j] \cdot \mathbf{n} = 0, \quad (3.1)$$

while the RH condition associated to the  $j$ th momentum is

$$[h_j \mathbf{v}_j]n_t + [h_j \mathbf{v}_j (\mathbf{v}_j \cdot \mathbf{n})] + g \langle h_j \rangle [s^{j-1} h_1 + h_2] \mathbf{n} = 0, \quad (3.2)$$

where  $\langle \dots \rangle$  denotes the half sum of the values of a quantity on each side of the discontinuity. Observe that the sum over  $j$  of (3.2) times  $\rho_j$  gives the RH condition associated to the total momentum,

$$\left[ \sum_j \rho_j h_j \mathbf{v}_j \right] n_t + \left[ \sum_j \rho_j \left( h_j \mathbf{v}_j (\mathbf{v}_j \cdot \mathbf{n}) + g \frac{h_j^2}{2} \mathbf{n} \right) + \rho_1 g h_1 h_2 \mathbf{n} \right] = 0. \quad (3.3)$$

The consistency with these RH conditions, however, does not ensure full convergence, and means only that we have a good approximation (the continuity equations, total momentum equation and energy inequality are enforced nevertheless). A comprehensive study on the behaviour of shock capturing numerical approximations of the two-layer rotating shallow-water model system in the presence of shocks is given in Castro *et al.* (2008), where it is explained that one can hardly do better. A way to check the relevance of the solution is to compare the two-layer simulations, in the limit of large difference in the densities of the layers and/or small upper to lower layer depth ratio, with the single layer ones. Such calculations give quasi-identical results (not shown). Thus, all calculations below correspond to approximate layerwise momentum conservation across the shocks, with exact total momentum conservation, and the energy decrease, which should not be forgotten while physically interpreting the results. At the same time, to our knowledge, no consistent numerical scheme with non-standard RH conditions exists for the two-layer system. The calculations below may also be considered as a test for the new code, which it successfully passed.

### 3.2. Nonlinear evolution of a barotropically stable flow

#### 3.2.1. Baroclinic instability

We will first consider the basic flow with zero velocity at the wall, see height and velocity profiles in figure 2. This corresponds to the barotropically stable flow studied in §2.3.

We simulate the fully nonlinear evolution of the instability corresponding to the most unstable mode (RF) (figure 6a) with  $k_0 = 0.98$  for the basic state with  $r = 2$  and  $s = 0.5$  (cf. figure 3c). Note that, we also performed simulations with different  $s$  and  $r$  while keeping the same ratio  $r/s = 4$ , and obtained similar results. The



boundary conditions are periodic in the zonal direction, with the period  $2\pi/k_0$ , and we initialize the simulation with the most unstable  $x$ -periodic eigenmode obtained from the linear stability analysis. The allowed wavenumbers are then integer multiples of  $k_0$ . Note that this wavenumber has been chosen in order to allow also for the RP instability which has a wavenumber  $\approx 6k_0$  (cf. figure 3). The spatio-temporal evolution of the instability is displayed in figure 11 and the growth of kinetic energy for the most energetic  $k = k_0$  mode is presented in figure 12 for both layers. The unstable RF mode grows exponentially until  $t = 125$  with an average growth rate  $\sigma \approx 0.02$  leading to the formation of baroclinic vortices. Strong events of dissipation happen at  $150 < t < 200$ , essentially near the wall (see figure 11(c, c'), where the small white areas superimposed on the isolines of the height field correspond to the spatial distribution of the dissipation rate). While the vortex develops, a local return current appears close to the wall, and a Kelvin front forms and breaks leading to shock formation and enhanced dissipation, as was explained in Part 1 (cf. a zoom of this event in figure 13). The small-scale motions in the lower layer at this stage are presented in figure 14, where the pressure and velocity fields of the main vortex have been filtered out. They correspond to inertia-gravity wave emission by the Kelvin front, and the adjustment of the vortex. The dissipation due to the Kelvin front leads to reconnection of the vorticity isolines allowing for vortex detachment from the mean flow and its subsequent offshore motion. Figure 15(a) displays the pressure distribution in both layers at  $t = 250$ , when the vortex is well formed and detaches. It is the dipolar structure of the lower-layer vortex, which drives it offshore. We present the cross-section of the detaching vortex in figure 15(b), where its lens-like structure is clearly seen.

The total energy loss during the whole simulation is about 0.03 % of the total initial energy or 25 % of the initial kinetic energy, as shown in figure 16. It is non-negligible, but stays quite acceptable compared to the rather long duration ( $t = 500$ ) of the simulation. In the numerical scheme we are using, the numerical dissipation acts only in the zones of high gradients. The events of enhanced dissipation take place during the detachment of the vortex, which is consistent with what was stated above. The slow monotonic decrease of energy during the whole simulation is explained by the fact that it is easy to generate micro shocks in the shallow regions where the upper layer is close to drying.

We have also directly simulated the nonlinear stage of the second and the third instability zones of the phase diagram of figure 3(b, c) corresponding to the resonances between a vortical mode in the lower layer and Poincaré modes of different orders in the upper layer (figure 6b). These modes, as well as even higher- $k$  unstable modes have high gradients close to the initial front and thus are likely to be damped owing to dissipation as occurs in the problem of instabilities of coupled density fronts (cf. Scherer & Zeitlin 2008). Indeed, we observed a rapid energy decay at the initial stage of the simulation. The growth of such unstable modes is almost immediately arrested and they are hence unable to change the structure of the background flow, contrary to the main instability mode. After some time the perturbation eventually leads to the development of the aforementioned baroclinic instability. This means that in the context of long-time nonlinear evolution of coastal currents, the only relevance of these high wavenumber modes is to provide a dissipative sink of energy.

### 3.2.2. Joint evolution of vertical shear and RF instabilities

In order to study the effect of the loss of hyperbolicity in the equations and its link to vertical shear instability, we repeat the previous simulation with the depth ratio

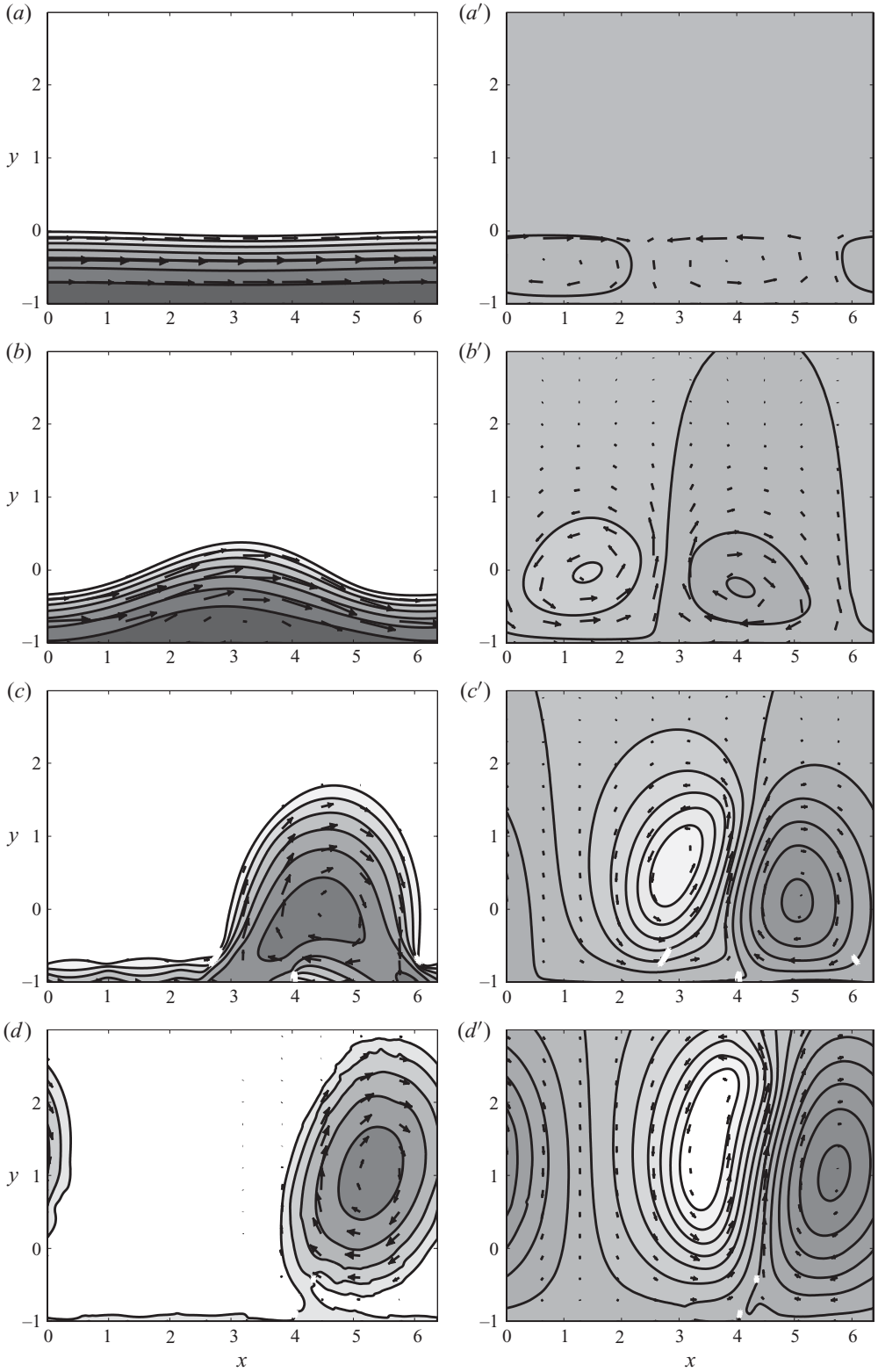


FIGURE 11. For caption see facing page.

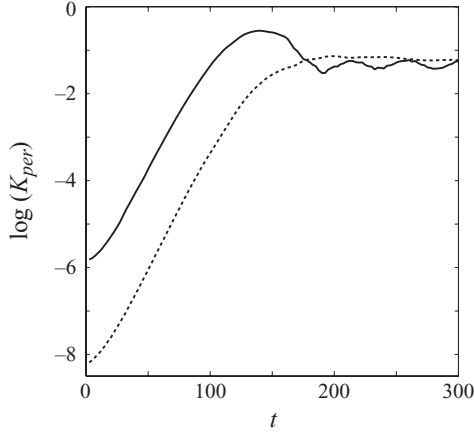


FIGURE 12. Logarithm of the kinetic energy,  $K_{per}$ , of the perturbation for the simulation of figure 11 (normalized by initial total kinetic energy) for mode  $k = k_0$  in the upper layer (thick line) and in the lower layer (dashed line).

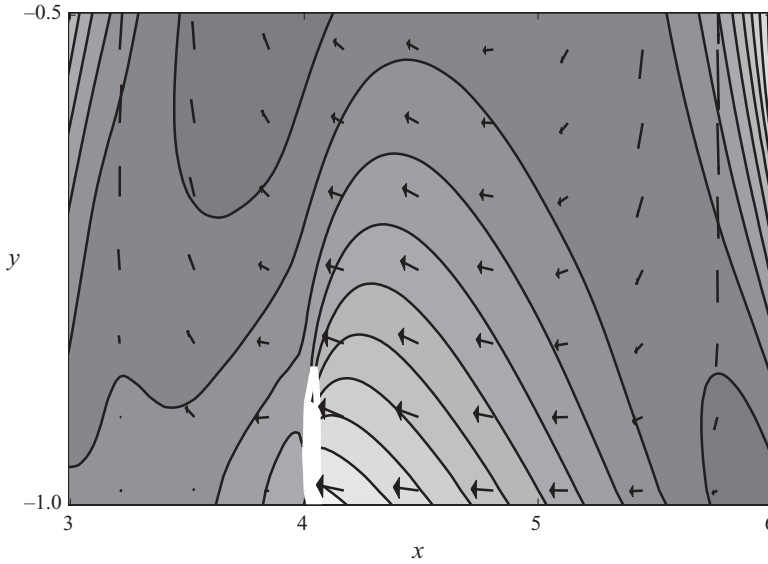


FIGURE 13. Zoom of figure 11(c).

lowered down to  $r = 0.5$ . According to the linear stability analysis (figure 3d), the most unstable modes are now vertical shear instability modes (PF in figure 6d) with typical wavenumbers  $k > 20$ , while the RF instability (figure 6a) is still supposed to develop, but at a wavenumber  $k = 1.4$ , and with a lower growth rate as can be seen in the phase diagram.

FIGURE 11. Levels of  $h_1(x, y, t)$  in the upper layer ( $a-d$ ) and isobars of  $\pi_2(x, y, t)$  in the lower layer ( $a'-d'$ ) at  $t = 0, 100, 150$  and  $200$ , respectively ( $a, a'$ ), ( $b, b'$ ), ( $c, c'$ ) and ( $d, d'$ ), for the development of the unstable RF mode superposed on the basic flow with a depth ratio  $r = 2$  and density ratio  $s = 0.5$ . Contours at interval 0.1 for  $h_1(x, y, t)$  ( $a-d$ ) and 0.01 for  $\pi_2(x, y, t)$  ( $a'-d'$ ). Darker (lighter) zones correspond to positive (negative) anomalies of  $\pi_2$  in ( $a'-d'$ ). The arrows indicate the mass flux  $h\mathbf{v}$ . The initial amplitude of the perturbation is 10%. Dissipation zones (at more than 10% of the max value of the dissipation rate) are marked by small white areas superimposed on the contours.

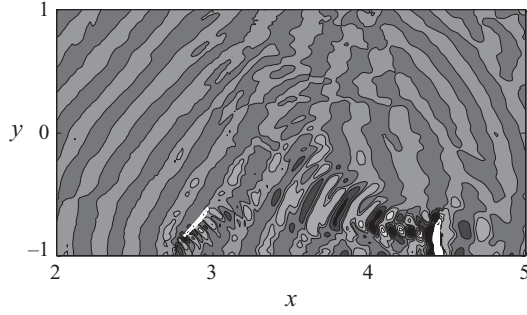


FIGURE 14. Isobars of  $\pi_2(x, y, t)$  in the lower layer at  $t = 160$  with mean zonal flow filtered out for the simulation of figure 11. Only the modes with  $k > 10$  are represented.

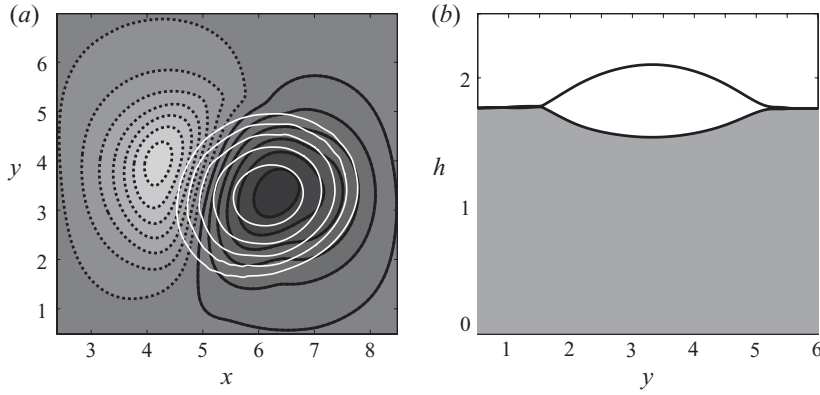


FIGURE 15. Isobars of  $\pi_1(x, y, t)$  in the upper layer (white lines) and  $\pi_2(x, y, t)$  in the lower layer (dark lines) (a) and  $y$  cross-section (b) of the detached vortex at  $t = 250$  for the simulation of figure 11. Dark (light) background in (a): anticyclonic (cyclonic) region.

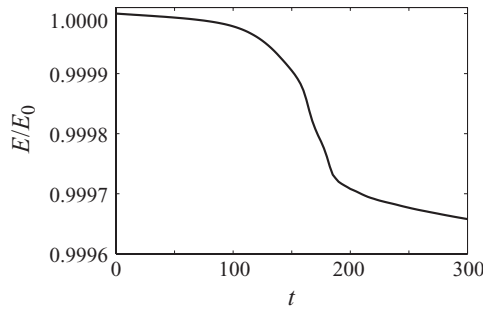


FIGURE 16. Time-dependence of the total energy normalized by the initial energy for the evolution of the instability.

Figure 17 shows the result of nonlinear evolution of the instability corresponding to the unstable RF mode with  $k_0 = 1.4$  superimposed onto the basic flow. The zonal period is chosen to be  $2\pi/k_0$  in non-dimensional units.

Looking at figure 17(a') and at the evolution of the kinetic energy  $K_{per}$  of the perturbation presented in figure 18(a), we see that short-wave structures are growing

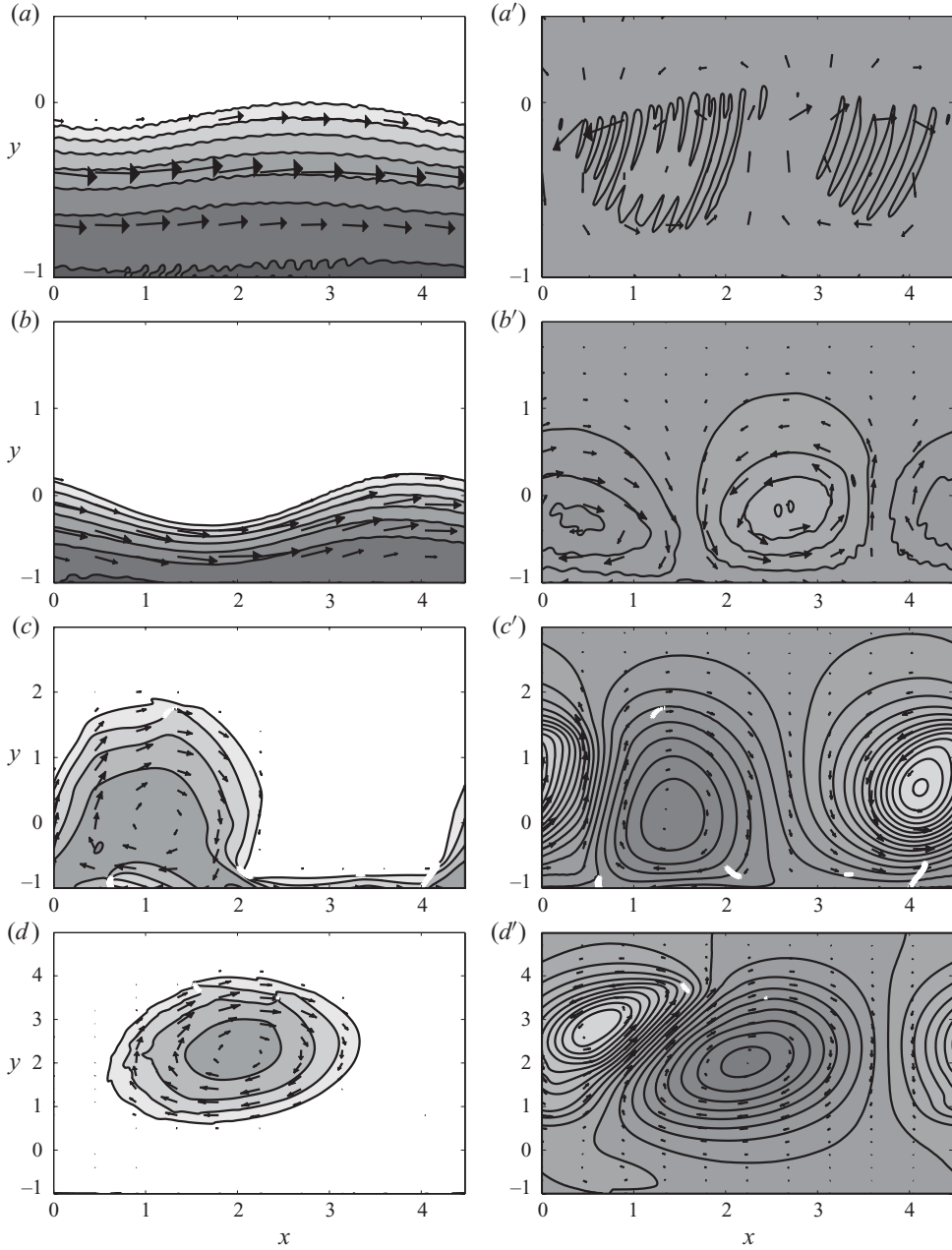


FIGURE 17. Levels of  $h_1(x, y, t)$  in the upper layer ( $a-d$ ) and isobars of  $\pi_2(x, y, t)$  in the lower layer ( $a'-d'$ ) at  $t = 10, 30, 60$  and  $110$ , respectively ( $a, a'$ ), ( $b, b'$ ), ( $c, c'$ ) and ( $d, d'$ ), for the development of an initial perturbation superposed on the basic flow with a depth ratio  $r = 0.5$ . Same conventions as in figure 11.

very fast during the earlier stage of the simulation ( $t < 20$ ). The pressure and velocity fields of the corresponding perturbation are plotted in figure 19( $a, a'$ ) and fit well the vertical-shear-instability mode structure obtained from the linear stability analysis (cf. figure 6d). From figure 19( $b$ ), where we plotted the energy spectrum of the flow

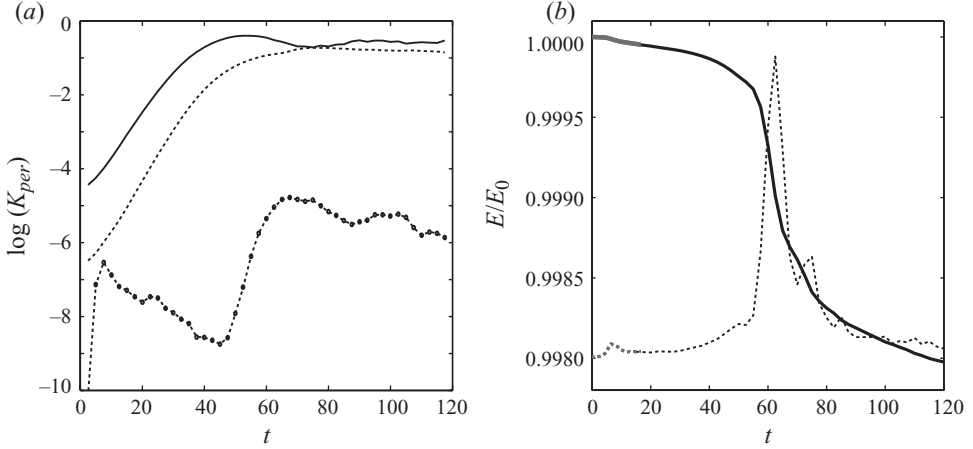


FIGURE 18. (a) Logarithm of the kinetic energy,  $K_{per}$ , (normalized by initial total kinetic energy) of the perturbation for the simulation of figure 17 for mode  $k=k_0$  in the upper layer (thick line) and in the lower layer (dashed line), and for the sum of modes with  $k > 10 k_0$  (dashed-dotted line). (b) Time-dependence of the total energy normalized by the initial energy (thick line) and the dissipation rate (dashed line) for the evolution of the instability of figure 17.

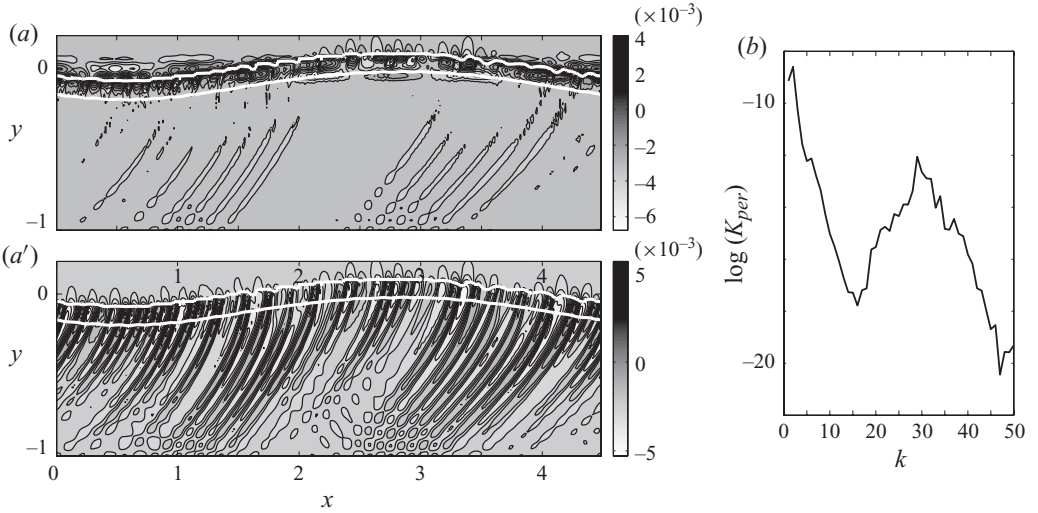


FIGURE 19. (a, a') Contours of  $\pi_1(x, y, t)$  (a) and  $\pi_2(x, y, t)$  (a') with mean zonal flow filtered out (only modes with  $k > 4 k_0$  are represented) at  $t=20$  for the simulation of figure 17 with a depth ratio  $r=0.5$ . The white lines indicate the boundaries of non-hyperbolic domains. (b) Normalized kinetic energy spectrum at  $t=20$  after development of the small-scale vertical shear instabilities in the simulation of figure 17.

at  $t=20$ , we can see that the short-wave maximum is centred at  $k \approx 29$ . We can deduce that this mode has the growth rate  $\sigma \approx 0.5$ , which is consistent with the results of the linear stability analysis (see figure 3d). Our numerical scheme allows the diagnosis of the loss of hyperbolicity, which is related to a vertical shear instability, as was explained earlier. The domains where the loss of hyperbolicity is encountered

are indicated in figure 19(a, a') which confirms their link with the vertical shear instability due to the PF resonance. Note that the numerical solution comes back to the hyperbolic regime by itself after having displayed a non-hyperbolic behaviour.

As we see, the small-scale vertical shear instabilities do not qualitatively alter the flow, their only influence is to render it marginally stable to shear instability through enhanced dissipation in the strong vertical shear regions. The mean current then develops secondary large-scale instabilities at  $k = k_0$ . The evolution is similar to the previous case of  $r = 2$ , except that, due to the thinner lower layer, the phase speed of the vortex waves in the lower layer increases, while the phase speed of the frontal wave remains the same, which makes the growth rate and wavenumber corresponding to the maximum growth rate increase (see figure 3 for comparison). The growth rate of this instability measured from the kinetic energy evolution is  $\sigma \approx 0.1$ , the instability then grows about three times faster than in the  $r = 2$  case.

The total energy loss during the whole simulation is about 0.2 % of the total initial energy or 25 % of the initial kinetic energy as shown in figure 18(b). The events of enhanced dissipation take place during the appearance of vertical shear instabilities (first peak of dissipation at  $t \approx 10$ ) and during the detachment of the vortex ( $t \approx 60$ ). Consistently with what was stated above, the overall dissipation during the saturation of small-scale vertical shear instabilities is much less important than the dissipation during the saturation of the large-scale RF instability.

### 3.3. Nonlinear evolution of a barotropically unstable flow

In the previous section the upper-layer KF instability, studied in Part 1, was excluded. A natural question arises regarding how the presence of the baroclinic instabilities changes the evolution of this instability. We describe below a joint evolution of the RF and upper-layer KF instability (KF1).

We simulate the fully nonlinear evolution of the instability corresponding to the most unstable mode with  $k = 3.44$ , as given by the linear stability analysis (cf. figure 9a) in a similar way as in Part 1, but with the addition of an active lower layer. As expected from the linear stability analysis (figure 8a), configurations with a very large depth ratio ( $r > 100$ ), give absolute coincidence with the previous simulations in the reduced-gravity configuration. When the depth ratio is reduced to  $r = 2$ , baroclinic effects modify the flow. The stability diagram (figure 8c) shows that even if the most unstable mode is still the upper-layer KF mode, some baroclinic instabilities also appear. The evolution of the flow in this case is shown in figure 20 and displays two different stages. The first stage ( $t < 250$ , shown in figures 20a, a' and 20b, b') is close to reduced-gravity simulations of Part 1: the unstable mode grows, saturates and modifies the mean flow (figure 20a, a'), then a secondary instability grows and breaks (figure 20b, b') by reorganizing the flow.

The next stage of the evolution of the flow in both layers is shown in figure 20 for  $t > 250$ . As we have seen in Part 1, the final state for the one-layer flow simulation exhibited a Rossby wave-like pattern, with coherent vortices located near the coast inside meanders of the main current. As an active lower layer is now present, it will allow for interactions of such patterns with the vortical modes of the lower layer. In a similar way as for the barotropically stable flow discussed in the previous section (figure 11), a baroclinic instability will then develop. Figure 20 shows the baroclinic interactions which lead to the formation of a vortex in the upper layer and of a dipole with a cyclone followed by an anticyclone in the lower layer, that detaches from the coast. Formation of cutoff vortices is clearly seen. As before it is the dipolar structure

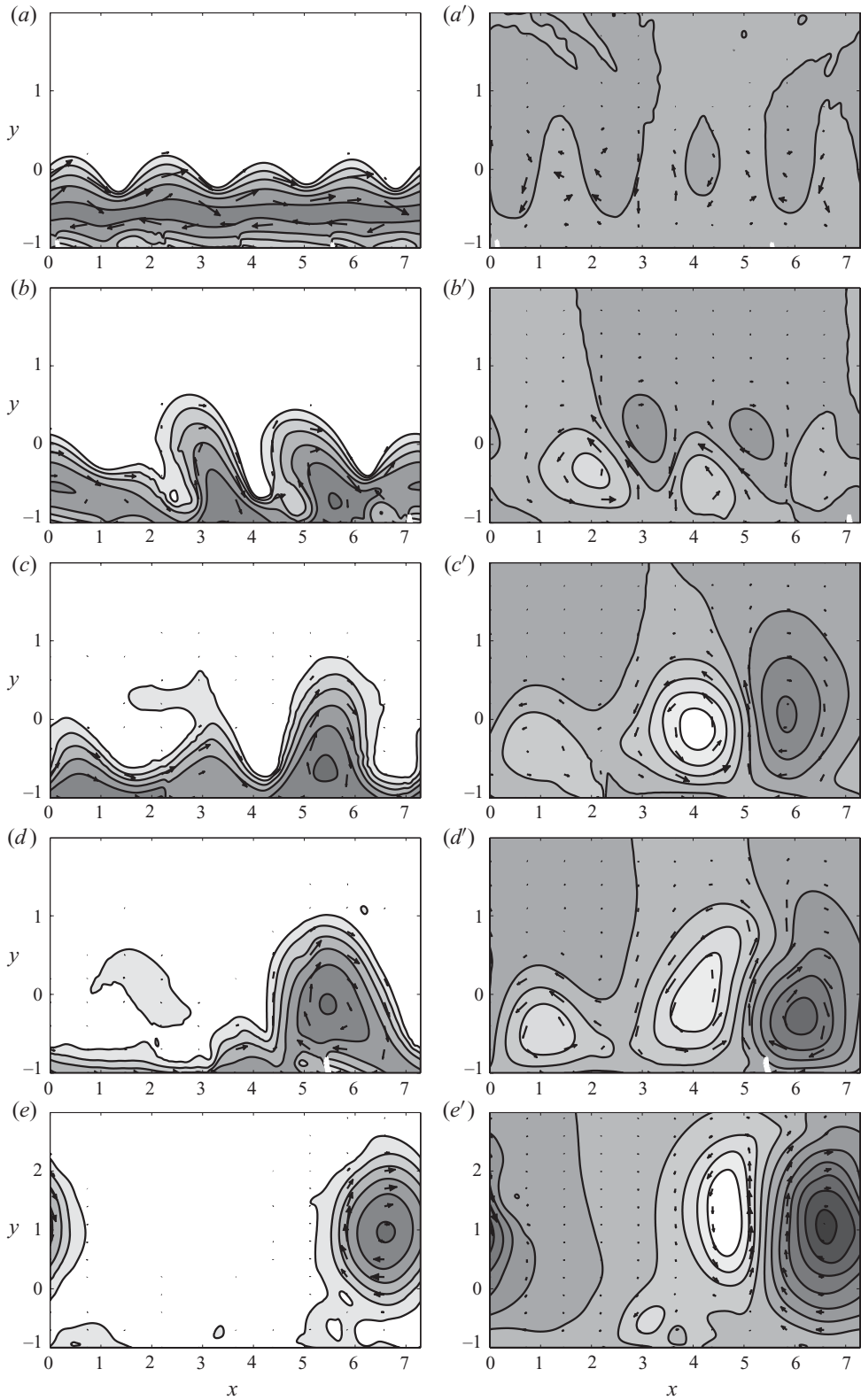


FIGURE 20. For caption see facing page.



in the lower layer which is driving them offshore. We present the evolution of PV in both layers in this simulation in figure 21.

It should be noted that the evolution of the BDCC we observe here was quite foreseeable: with a deep lower layer the interaction between the two layers is rather weak and the rapid upper-layer KF instability is dominant at the beginning. Baroclinic effects, as usual, come into play on longer time scales.

The evolution of the kinetic energy of the different perturbation modes in the upper layer presented in figure 22 is to be compared with that of the one-layer case (see figure 20 in Part 1) and, as expected, is quite similar for  $t < 200$ . The total kinetic energy of the perturbation in the lower layer is also presented in figure 22. It is initially zero, but is increasing throughout the simulation until the flow becomes clearly baroclinic.

The total energy loss during the whole simulation is about 0.08 % of the total initial energy or 50 % of the initial kinetic energy, as shown in figure 23. The events of enhanced dissipation take place during the breaking of the Kelvin mode (first peak of dissipation at  $t \approx 25$ ), during the breaking of the secondary unstable wave ( $t \approx 150$ ) and finally during the detachment of the vortex ( $t \approx 300$ ).

We also studied a joint evolution of vertical shear, RF and upper-layer KF instabilities, by lowering the depth ratio. In short, the evolution of the flow is as follows (we do not give corresponding figures, which can be produced on request).

As expected from the linear stability analysis, vigorously growing short-scale instabilities at the front develop during the early stages of the simulation. The kinetic energy of the short-scale modes is growing very fast at initial stages, with substantial growth rates. The corresponding unstable short-wave mode clearly shows the similarity with the linearly unstable mode of figure 6, with a coupled short-wave Poincaré mode in the lower layer and short-wave frontal mode in the upper layer.

The vertical shear instabilities enhance dissipation but, as in the case of barotropically stable flow, do not significantly alter the mean flow. The unstable frontal mode (upper-layer KF resonance) keeps on growing with a weak growth rate compatible with the linear stability analysis. The Kelvin and frontal modes grow until the Kelvin mode breaks and modifies the mean flow along the coast, in a similar way as in the simulations of Part 1. The secondary unstable mode, also described in Part 1, then appears in the upper layer in the form of a pair of Rossby waves at each side of the current. Contrary to the preceding simulations with larger depth ratio, the coupling between the two layers is much more important, and the Rossby wave excited in the lower layer is strongly interacting with the upper layer one. The breaking of the unstable mode in the upper layer is then quite different, as it leads to quick formation of smaller vortices.

The total energy loss during the whole simulation is, again, rather limited. The events of enhanced dissipation take place during the appearance of vertical shear instability, during the breaking of the Kelvin mode and during detachment of vortices from the coast.

---

FIGURE 20. Levels of  $h_1(x, y, t)$  ( $a-e$ ) and  $\pi_2(x, y, t)$  ( $a'-e'$ ) at  $t = 110, 130, 250, 300$  and  $500$ , respectively ( $a, a'$ ), ( $b, b'$ ), ( $c, c'$ ), ( $d, d'$ ) and ( $e, e'$ ), for the development of the most unstable mode of figure 9(a), corresponding to the basic flow with constant PV and a depth ratio  $r = 2$ . Contours at interval 0.05 for  $h_1(x, y, t)$ , and 0.005 for  $\pi_2(x, y, t)$ . The calculation domain is periodic in the  $x$ -direction and corresponds to four wavelengths of the most unstable mode. Same conventions as in figure 11.

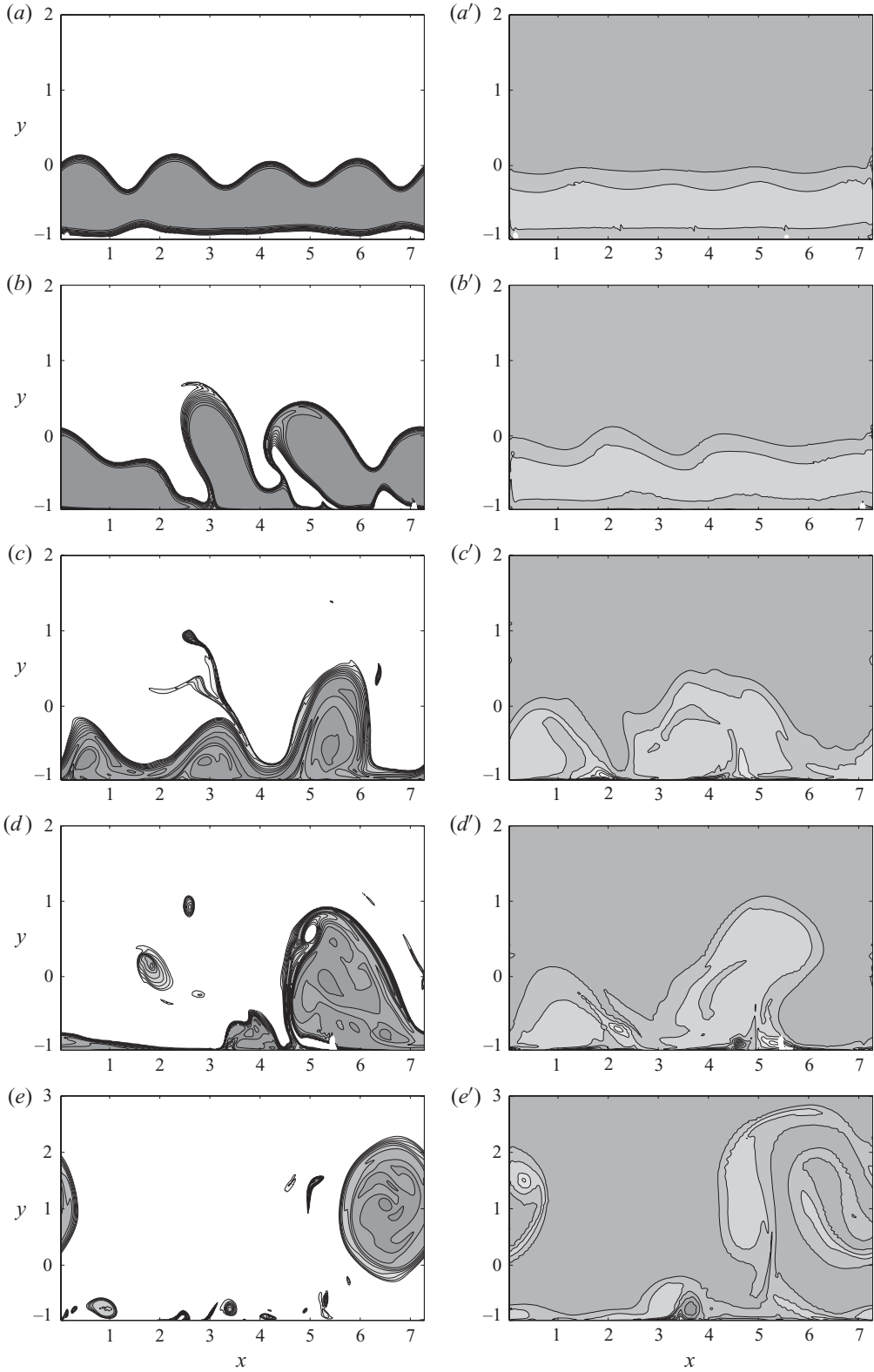


FIGURE 21. For caption see facing page.

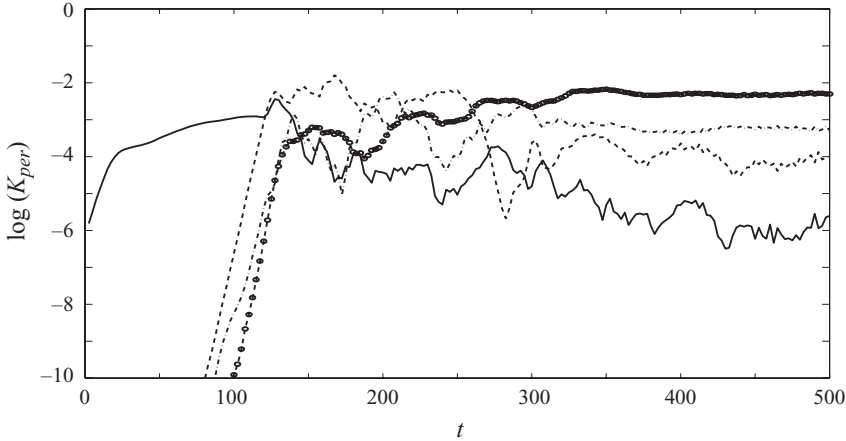


FIGURE 22. Logarithm of the kinetic energy,  $K_{per}$ , (normalized by initial total kinetic energy) of the perturbation for the simulation of figure 20 for mode  $k=k_0$  in the upper layer (thick line), mode  $k=0.75 k_0$  in the upper layer (dashed line), mode  $k=0.5 k_0$  in the upper layer (dash-dotted line) and the total kinetic energy of the perturbation in the lower layer (round markers), as a function of time.

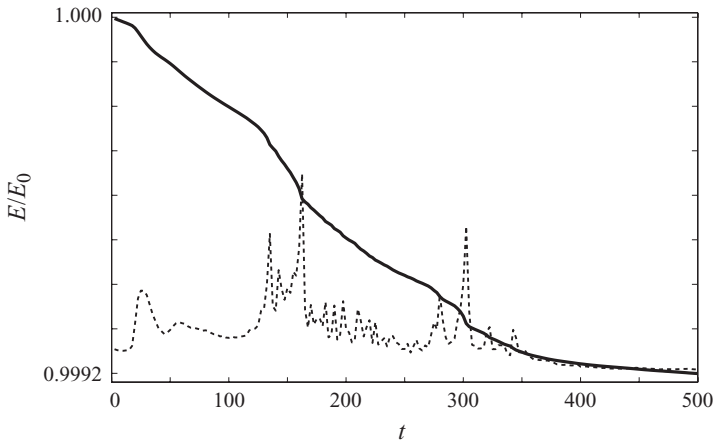


FIGURE 23. Time evolution of the total energy (continuous line) normalized by the initial energy, and dissipation rate (dashed) for the simulation of figure 20.

#### 4. Summary and conclusions

We have investigated linear and nonlinear stability of BDCC in the two-layer rotating shallow water model and generalized the results obtained for the reduced-gravity one-layer model of Gula & Zeitlin (2010). We presented the results of an exhaustive linear stability analysis of, respectively, configurations with stable or unstable, in the barotropic (reduced-gravity, one-layer) limit, upper-layer current.

FIGURE 21. Contours of PV for the simulation of figure 20 in the upper layer ( $a-e$ ) and in the lower layer ( $a'-e'$ ) for  $t=110, 130, 250, 300$  and  $500$ , respectively ( $a, a'$ ), ( $b, b'$ ), ( $c, c'$ ), ( $d, d'$ ) and ( $e, e'$ ). Contours at the interval 1 for PV in the upper layer and at the interval 0.1 for PV in the lower layer.

The linear instabilities were identified and classified according to the character of resonating waves forming the unstable modes, and their dependence on the depth ratio of the layers was displayed. The fully nonlinear DNS using a novel high-resolution entropy-satisfying well-balanced finite-volume scheme of Bouchut & Zeitlin (2010), which copes with losses of hyperbolicity associated to shear (KH type) instabilities in multi-layer systems, were performed to understand the nonlinear stage of instability.

The main conclusions following from these DNS are as follows. In the case of barotropically stable upper-layer flow for deep, but not extremely deep, lower layers the baroclinicity destabilizes the system via an instability due to the resonance between the lower-layer Rossby wave and an upper-layer frontal wave propagating along the outcropping line (RF instability). The growing RF instability leads to breaking of the Rossby and the frontal wave in the respective layers, and formation of coherent vortices which are able to detach from the coast due to their dipolar structure in the lower layer. Kelvin front formation at the coast plays an important role in this process. For sufficiently shallow lower layers, the short-wave shear instabilities dominate the initial evolution of the flow. They are, however, rapidly smeared out by dissipation, and do not lead to substantial reorganization of the flow, which is then subject to the RF instability with similar, as described above, evolution.

In the case of barotropically unstable upper-layer flow, and sufficiently deep lower layers, the instability resulting from the resonance of the frontal and Kelvin waves in the upper layer (KF instability), dominates following the scenario of Part 1. However, at the later stages of the evolution the baroclinic RF instability steps in and excites vortex structures in the lower layer. The whole system then undergoes baroclinic instability leading to coherent vortices appearing in both layers and eventually detaching from the coast. For shallower lower layers, again, the shear instabilities dominate at initial stages, being eliminated then by dissipation. They do not much influence the development of the upper-layer KF instability, and subsequent switching of slower RF baroclinic instability. This latter leads to the formation of coherent vortices with pronounced baroclinic structure.

Let us finally mention that the linear stability analysis exposed in this paper and in Part 1 may be performed in cylindrical geometry used in experimental studies (cf. Griffiths & Linden 1982), as was done by Gula, Zeitlin & Plougonven (2009*b*) for non-outcropping configurations, with results similar to those presented above.

This work was supported by ANR project FLOWING (BLAN06-3 137005) and Alliance project 15102ZJ.

#### REFERENCES

- BARTH, J. A. 1989 Stability of a coastal upwelling front. Part 1. Model development and a stability theorem. *J. Geophys. Res.* **94**, 10844–10856.
- BOSS, E., PALDOR, N. & THOMPSON, L. 1996 Stability of a potential vorticity front: from quasi-geostrophy to shallow water. *J. Fluid Mech.* **315**, 65–84.
- BOUCHUT, F., LE SOMMER, J. & ZEITLIN, V. 2004 1D rotating shallow water: nonlinear semi-geostrophic adjustment, slow manifold and nonlinear wave phenomena. Part 2. High-resolution numerical simulations. *J. Fluid Mech.* **514**, 35–63.
- BOUCHUT, F. & MORALES, T. 2008 An entropy satisfying scheme for two-layer shallow water equations with uncoupled treatment. *M2AN* **42**, 683–698.
- BOUCHUT, F. & ZEITLIN, V. 2010 A robust well-balanced scheme for multi-layer shallow water equations. *Discrete Continuous Dyn. Syst. B* **13**, 739–758.
- CAIRNS, R. A. 1979 The role of negative energy waves in some instabilities of parallel flows. *J. Fluid Mech.* **92**, 1–14.

- CASTRO, M. J., LEFLOCH, P. G., MUNOS-RUIZ, M. L. & PARÉS, C. 2008 Why many theories of shock waves are necessary: convergence error in formally path-consistent schemes. *J. Comput. Phys.* **227**, 8107–8129.
- GRIFFITHS, R. W. & LINDEN, P. F. 1982 Part I. Density-driven boundary currents. *Geophys. Astrophys. Fluid Dyn.* **19**, 159–187.
- GULA, J., PLOUGONVEN, R. & ZEITLIN, V. 2009a Ageostrophic instabilities of fronts in a channel in the stratified rotating fluid. *J. Fluid Mech.* **627**, 485–507.
- GULA, J. & ZEITLIN, V. 2010 Instabilities of buoyancy-driven coastal currents and their nonlinear evolution in the two-layer rotating shallow water model. Part 1. Passive lower layer. *J. Fluid Mech.* **659**, 69–93.
- GULA, J., ZEITLIN, V. & PLOUGONVEN, R. 2009b Instabilities of two-layer shallow-water flows with vertical shear in the rotating annulus. *J. Fluid Mech.* **638**, 27–47.
- HOSKINS, B. J., MCINTYRE, M. E. & ROBERTSON, A. W. 1985 On the use and significance of isentropic potential vorticity maps. *Q. J. R. Meteorol. Soc.* **111** (470), 877–946.
- IGA, K. 1997 Instability of a front with a layer of uniform potential vorticity. *J. Meteorol. Soc. Japan* **75**, 1–11.
- KILLWORTH, P. D., PALDOR, N. & STERN, M. E. 1984 Wave propagation and growth on a surface front in a two-layer geostrophic current. *J. Mar. Res.* **42**, 761–785.
- KLEMP, J. B., ROTUNNO, R. & SKAMAROCK, W. C. 1997 On the propagation of internal bores. *J. Fluid Mech.* **331**, 81–106.
- KUBOKAWA, A. 1988 Instability and nonlinear evolution of a density-driven coastal current with a surface front in a two-layer ocean. *Geophys. Astrophys. Fluid Dyn.* **40**, 195–223.
- LEBLOND, P. H. & MYSAK, L. A. 1978 *Waves in the Ocean*. Elsevier.
- LESOMMER, J., MEDVEDEV, S., PLOUGONVEN, R. & ZEITLIN, V. 2003 Singularity formation during relaxation of jets and fronts towards the state of geostrophic equilibrium. *Commun. Nonlinear Sci. Numer. Simul.* **8**, 415–442.
- LYAPIDEVSKY, V. Y. & TESHUKOV, V. M. 2000 Mathematical models of long wave propagation in inhomogeneous fluid (in Russian). *Siberian Branch of the Russian Academy of Science, Novosibirsk*. ISBN: 5-7692-0340-4.
- PALDOR, N. & GHIL, M. 1991 Shortwave instabilities of coastal currents. *Geophys. Astrophys. Fluid Dyn.* **58**, 225–241.
- PALDOR, N. & KILLWORTH, P. D. 1987 Instabilities of a two-layer coupled front. *Deep-Sea Res.* **34**, 1525–1539.
- POULIN, F. J. & FLIERL, G. R. 2003 The nonlinear evolution of barotropically unstable jets. *J. Phys. Oceanogr.* **33**, 2173–2192.
- RIPA, P. 1991 General stability conditions for a multi-layer model. *J. Fluid Mech.* **222**, 119–137.
- SAKAI, S. 1989 Rossby–Kelvin instability: a new type of ageostrophic instability caused by a resonance between Rossby waves and gravity waves. *J. Fluid Mech.* **202**, 149–176.
- SCHERER, E. & ZEITLIN, V. 2008 Instability of coupled geostrophic density fronts and its nonlinear evolution. *J. Fluid Mech.* **613**, 309–327.
- TREFETHEN, L. N. 2000 *Spectral Methods in Matlab*. SIAM.
- WHITHAM, G. B. 1974 *Linear and Nonlinear Waves*. Wiley.